Stability and dissociation pathways of doped Au_nX^+ clusters (X = Y, Er, Nb)†

Nele Veldeman,[a] Ewald Janssens,[a] Klavs Hansen,[b] Jorg De Haeck,[a] Roger E. Silverans[a] and Peter Lievens*[a]

Received 19th April 2007, Accepted 4th May 2007
First published as an Advance Article on the web 14th September 2007
DOI: 10.1039/b705920e

Size dependent stabilities, fragmentation pathways and dissociation energies of a series of gas phase cationic doped gold clusters, Au_nX^+ ($3 \leq n \leq 20$; X = Y, Er and Nb), and pure Au_n^+ clusters were investigated in photofragmentation experiments. Size dependent stability patterns were obtained and the branching between monomer and dimer evaporation was studied. For bare gold, the competing neutral monomer and dimer evaporation channels were found to be in agreement with earlier studies. For doped clusters, monomer evaporation is the most likely fragmentation channel with the exception of $Au_{18}Y^+$ and $Au_{20}Y^+$ for which gold dimer evaporation is also observed. Relations between the evaporative activation energies and both the experimental abundances and the fragment yield were derived based on unimolecular rate constants. The dissociation energies from this analysis show an odd–even staggering and enhanced stabilities for certain cluster sizes, in agreement with simple electronic shell model predictions.

1. Introduction

Gold nanoclusters have attracted a lot of attention in recent years in particular due to the potential applications as catalytic particles.[1] The electronic properties and size dependent stability of gold clusters have been characterized by photoelectron spectroscopy, photoionization spectroscopy, photofragmentation, and collision-induced dissociation studies.[2–8] Quantum confinement of the gold valence 6s electrons produces stability patterns that to a first approximation can be described in terms of an electronic shell structure.[4,9] Closed electron shells appear if the number of delocalized electrons correspond to the so-called *magic numbers*: 2, 8, 18, 20, 34, 58, 92. These magic sizes were observed in different experimental studies.

Since the demonstration with ion mobility measurements that charged gold clusters are planar up to surprisingly large sizes,[10,11] also the geometric structures of gold clusters attracted a lot of attention.[12–14] A number of unexpected geometries have recently been discovered, such as tetrahedral Au_{20},[15,16] fullerene-like Au_{26},[17]

[a] *Laboratorium voor Vaste-Stoffysica en Magnetisme & INPAC—Institute for Nanoscale Physics and Chemistry, K.U.Leuven, B-3001, Leuven, Belgium. E-mail: peter.lievens@fys.kuleuven.be*
[b] *Department of Physics, Göteborg University, Göteborg SE-412 96, Sweden. E-mail: klavs@physics.gu.se*

† Electronic supplementary information (ESI) available: Metastable fragmentation pathways of Au_n^+, Au_nY^+, Au_nEr^+ (**n** = 3–20), and Au_nNb^+ (**n** = 3–14). See DOI: 10.1039/b705920e

Au_{32},[18] and Au_{50},[19] and hollow Au_n (n = 16–18) cages.[20] Even golden nanotubes have been predicted.[21]

Not only bare gold clusters, but also their transition metal doped[22–31] and carbon (or carbon cluster)[32] doped counterparts have been actively studied. A single transition metal atom can strongly interact with a small gold cluster and, for certain cluster sizes and number of valence electrons, have a strong influence on the electronic shell structure and/or the cluster geometry. Combined photofragmentation mass spectrometry and density functional theory studies on Au_n clusters doped with open 3d shell atoms (Sc, Ti, V, Cr, Mn, Fe, Co, Ni, and Zn), have shown that the planar structure can be stabilized by a dopant atom and that in particular six-electron species are more stable.[22–26] It was also predicted that a central transition metal atom stabilizes a golden cage structure if the number of valence electrons satisfies the 18-electron rule.[27,28] This explains the high abundance obtained in mass spectra for $Au_{16}Sc^+$, $Au_{16}Y^+$, $Au_{15}Ti^+$ (ref. 7 and 22) as well as the unique stability of the icosahedral $Au_{12}W$.[29–31]

The strength of the interaction between a dopant atom and the host cluster is determined by the size of the cluster (geometric stabilization) and the number of dopant valence electrons (electronic shell closure). The combined effect of these parameters is reflected in the total binding energy and the differential binding energy (dissociation energy). The clusters are intrinsically stable and some excess energy, provided by, *e.g.*, photoexcitation, is needed to induce fragmentation. After photoexcitation the internal energy is statistically distributed over the vibrational modes of the system within a time scale shorter than the experimentally relevant time scales in mass spectrometric studies. The result is that the cluster does not instantaneously dissociate, even if the excitation energy is above the dissociation threshold. The delayed fragmentation in these so-called unimolecular decomposition processes is characterized by several parameters intrinsic to the clusters, and by the fact that the clusters are evaporating freely in an evaporative ensemble.[33,34] By applying statistical models, which predict the unimolecular dissociation rate assuming energy partitioning over the various modes, the recorded fragmentation yields after a well defined time can be converted into dissociation energies.

The delayed fragmentation yield has been measured for a multitude of monometallic clusters composed of monovalent atoms: Li_n^+ (n = 4–42),[35] Na_n^+ (n = 5–40),[33] K_n^+ (n = 5–200),[36] Cu_n^+ (n = 2–17),[37] Cu_n^- (n = 2–8),[38] Ag_n^+ (n = 3–21),[39] Ag_n^- (n = 2–11),[40] Au_n^+ (n = 3–23),[2,41–43] and Au_n^- (n = 2–15).[44] These studies showed that for small and for odd-sized clusters, monomer and dimer decay are competing channels, while all even-numbered ionic clusters evaporate a neutral monomer. In contrast to the extensive amount of accumulated information on decay pathways of pure clusters, there is little information available on the influence of the composition on the decay pathways of mixed clusters. We are only aware of two recent studies on some size selected $Ag_nCo_m^+$ and Si_nCr clusters.[45,46]

In this work we study the dissociation pathways and size dependent stability of cationic Au_nX^+ (X = Y, Er and Nb, n = 5–20) clusters. Statistical models are used to determine the monomer and dimer dissociation energies from both the recorded abundances and the fraction of mass selected clusters that undergo delayed fragmentation in the time window of the experiment. The dopant elements Y, Er, and Nb have been chosen to extend our earlier work, using 3d dopant atoms,[22–24] towards 4d transition metal atoms (Y, Nb) and lanthanide (Er) dopants.

2. Experimental

The clusters are produced in a dual-target dual-laser vaporization source, which is extensively described elsewhere.[47] Two independent pulsed Nd:YAG lasers vaporize the surface of two translating rectangular plate targets. Helium gas is introduced into the source by a pulsed supersonic valve. Subsequently, the mixture of atoms, clusters and inert gas expands into the vacuum, resulting in a cold molecular cluster beam.

The source parameters are optimized to achieve gold clusters containing only one or a few dopant atoms. After passage through a skimmer, the cluster beam enters the extraction region of a reflectron time-of-flight (RTOF) mass spectrometer.

To study neutral species, charged particles are deflected out of the beam and the remaining neutral beam is irradiated with laser light stemming from an ArF excimer laser (λ = 193 nm). Depending on the laser fluence, roughly two regimes can be differentiated. In the low fluence regime (<0.5 mJpp cm^{-2}) multiphoton absorption is unlikely and clusters will be excited or ionized by absorption of one photon only. In the high fluence regime (>5 mJpp cm^{-2}) the clusters are heated by multiphoton absorption. Cooling occurs through fast sequential evaporation of atoms and larger fragments. The resulting photofragments reveal a size distribution with higher abundances for clusters with enhanced stability. Following acceleration in the extraction zone, the clusters are mass separated in the field free drift region of the RTOF mass spectrometer. During the drift period, metastable parent cluster ions can undergo further evaporation (metastable or delayed fragmentation) with parent and fragment particles proceeding at the center-of-mass velocity.[33] In the reflectron the clusters are decelerated, turned around, and reaccelerated resulting in spatial and temporal separation of fragments with different masses.

A mass gate, located in between the extraction zone and the reflectron, allows for mass selection and offers the possibility to determine the evaporation channels of size selected clusters. The pulsed mass gate consists of a plane of parallel wire segments, formed by two electrically isolated sets of wires, similar to the device developed by Vlasak *et al*.[48] If the two wire sets are held at the potential of the field free region, the ion beam, travelling orthogonal to the plane of wire segments, is unaffected (gate open). Applying opposite voltages of equal magnitude (250 V) on the set of wires results in an electrical field perpendicular to the ion velocity and deflection of the ions (gate closed). By holding the gate closed until an ion packet of interest is about to reach the selector and then pulse the opening of the gate for the duration of the passage time, mass selective ion transmission is obtained. The resolution of the mass selection is determined by the planarity of the parallel wire system, the rise and fall times of the pulsed field, and the position of the mass gate, which should be located in the time focus of the two-field extraction zone. Pulsed voltage switches (Behlke HTS 21-03) with a short rise and fall time of 15 ns are used and a mass selection resolution of $m/\Delta m$ = 60 at m = 1000 amu was obtained. The timing is controlled by precise delay generators (DG 535, Stanford Research Systems). For each cluster size the time delay is optimized and the gate is typically opened for 600 ns.

3. Stability patterns and fragmentation channels

The recorded mass spectra for photofragmented Au_n^+ and Au_nX^+ (X = Y, Er, Nb; n = 1–30) are shown in Fig. 1. The dotted lines mark the pure Au_n^+ clusters, peaks corresponding to singly doped Au_nX^+ species are connected by a solid line. Metastable fragmentation pathways of Au_nX^+ for n = 9–14 (X = Au, Er, Nb) and n = 11–14, 18, 20 (X = Y) are shown in Fig. 2. The evaporation channels over an extended size range (n = 3–20) can be found in the ESI.† From the recorded metastable fragmentation, relative monomer and dimer evaporation yields are deduced (see Fig. 3).

A. Au_n^+

The photofragmentation spectrum for Au_n^+ (Fig. 1a) exhibits a distinct stability pattern with intensity steps at n = 3, 9, 19 and 21, corresponding to 2, 8, 18 and 20 delocalized valence s electrons. These are the so-called magic numbers for simple metal clusters and are related to the completion of electron shells for delocalized valence electrons enclosed in a potential well, as described extensively in the literature.[4,9,22] In addition to clear drops in abundance after the magic sizes a clear odd–even staggering is visible.

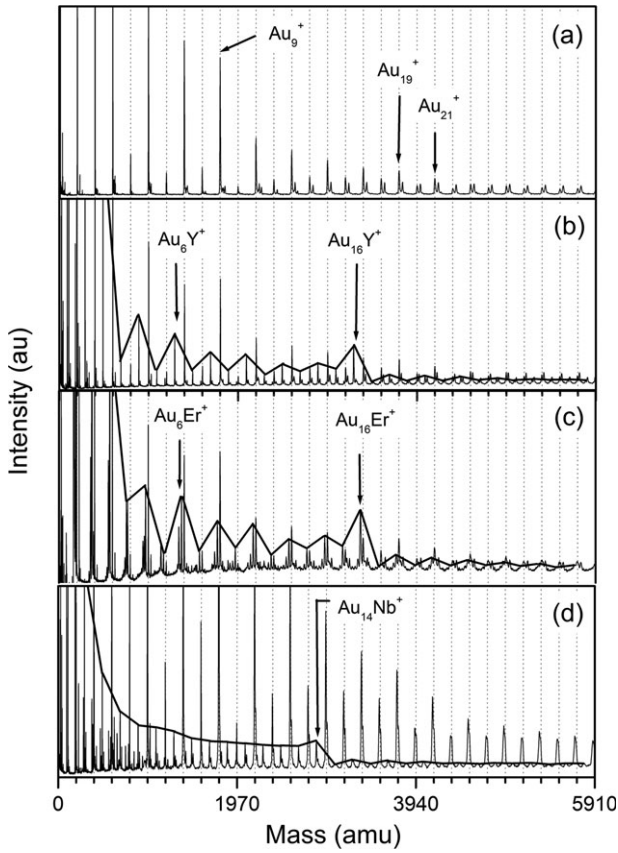

Fig. 1 Mass abundance spectra of photofragmented (a) Au_n^+, (b) Au_nY^+, (c) Au_nEr^+, and (d) Au_nNb^+ for $n = 1$–30. The grid lines mark the bare Au_n^+ clusters. Small peaks at the right side of the bare cluster peaks (mainly visible in panel (a)) correspond to metastable fragments stemming from one size up. Peaks corresponding to Au_nX^+ (X = Y, Er, and Nb) are connected by a solid line. Species after which there is a clear drop in abundance are labeled.

The delayed fragmentation pathways of mass selected Au_n^+ clusters (left column of Fig. 2) show a prominent peak, corresponding to the selected cluster (mother signal), and less intense peaks with a shorter flight time corresponding to metastable fragmentation (daughter peaks). The daughter clusters are created in the field free drift region and are separated in the reflectron when the electric field in the reflectron is detuned from the value which is optimal for mass spectrometric resolution. The fragmentation channels are indicated by labeled arrows. The preferred fragmentation channel is found to be size dependent.

The metastable fraction of monomer and dimer evaporation is shown as a function of the cluster size in Fig. 3a. For each mother cluster size n, the plotted values equal the integrated areas of respectively the monomer (■) and dimer (●) daughter peaks, divided by the total integrated area of the mother and daughter peaks.

For the smallest species ($n = 3$–5, 7) no delayed fragmentation is recorded. This is due to the combined results of three effects. First, the metastable fractions generally increase with cluster size. Secondly, the recoil energy upon dissociation is larger for small clusters, resulting in a poorer mass resolution, which makes the peaks more difficult to distinguish from the background. And thirdly, the beam path of daughter

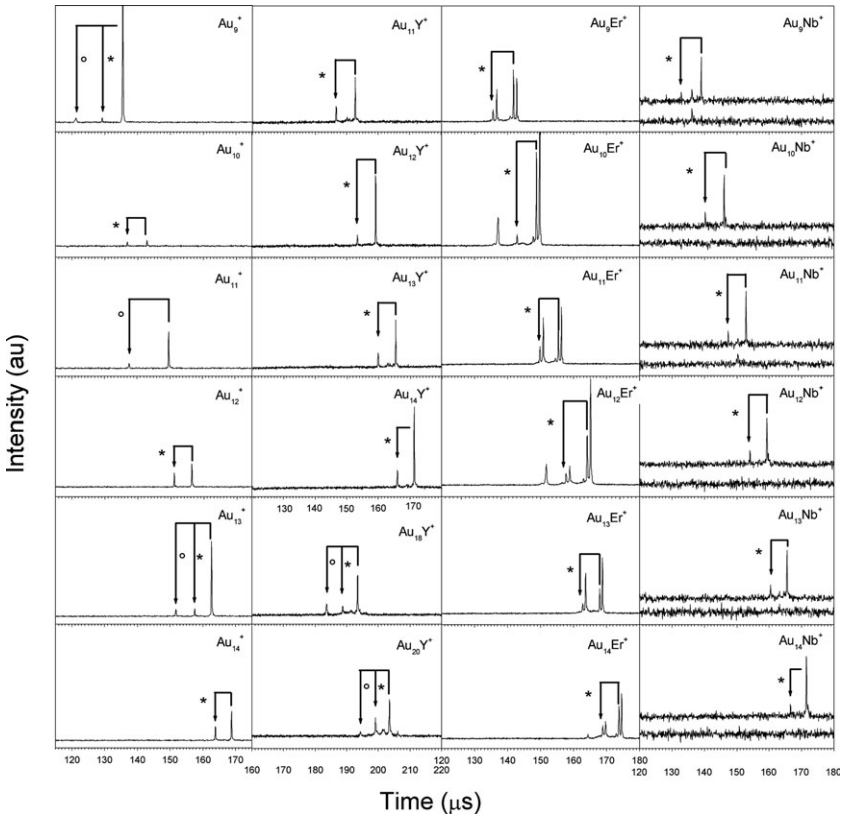

Fig. 2 Metastable fragmentation of Au_nX^+ for n = 9–14 (X = Au, Er, Nb) and n = 11–14, 18, 20 (X = Y). Because of the limited resolution of the mass selector for erbium doped gold clusters not only Au_nEr^+ was selected, but groups of $Au_{n+1}{}^+$, Au_nEr^+, $Au_{n-1}Er_2{}^+$ were transmitted. The dissociation channels (from parent to daughter) are indicated by arrows. Arrows labeled with * and ° correspond to neutral monomer and dimer evaporation, respectively. The bottom curves in the right column give the signal recorded as reference without any Nb in the clusters.

clusters deviates from the mother beam path after the reflectron. This deviation is larger for smaller clusters resulting in a loss of signal on the detector.

$Au_n{}^+$ ($n \geq 6$) clusters decay by neutral monomer dissociation with the exception of $Au_9{}^+$, $Au_{11}{}^+$, and $Au_{13}{}^+$, for which the main recorded dissociation channel is the evaporation of a gold dimer. For $Au_{15}{}^+$, dimer evaporation is observed but not as the main dissociation channel. Not only the preferred dissociation channel but also the dissociation probability strongly depends on the cluster size. The relative probability for monomer decay is higher for $Au_n{}^+$ with n even compared to their neighbors. Dimer evaporation however is more likely to occur for $Au_n{}^+$ with n odd. These results agree with photodissociation and collision induced dissociation experiments on size-selected $Au_n{}^+$ (n = 2–27) clusters in a Penning trap by Schweikhard *et al.*,[41–43] with the exception that we do not observe delayed fragmentation of the smallest clusters due to the above mentioned effects.

B. Au_nY^+

The photofragmentation spectrum for Au_nY^+ (Fig. 1b) exhibits strong finite size effects in agreement with an earlier study on yttrium doped gold clusters where the

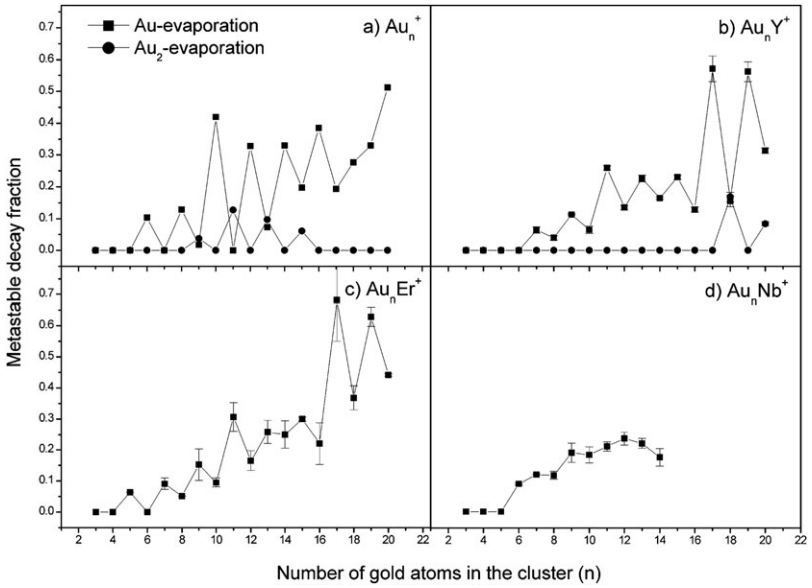

Fig. 3 Metastable decay fraction of neutral gold monomer and dimer evaporation pathways for (a) Au_n^+, (b) Au_nY^+, (c) Au_nEr^+, and (d) Au_nNb^+.

observed stability patterns, shell closures and odd–even effects were thoroughly discussed.[7] Prominent intensity steps can be observed at $n = 6$, 16 and 32 (32 not shown in the figure). Odd–even intensity alternations are present up to $n \approx 25$.

The evaporation channels recorded for metastable Au_nY^+ ($n = 11$–14, 18, 20) are shown in the second column of Fig. 2. From the labeled dissociation pathways it can be seen that the fragmentation channels, as for pure gold, are size dependent. The metastable fractions for monomer and dimer decay, deduced from the recorded delayed fragmentation spectra, are shown in Fig. 3b. The average is taken over three independent measurements, yielding reproducible ratios of the daughter-to-mother peak intensities. Error bars are statistically determined and correspond to the standard deviation of the average throughout. As for pure gold clusters, no delayed fragmentation is recorded for the smallest species ($n < 7$). Au_nY^+ ($n \geq 7$) clusters decay by monomer evaporation. For $Au_{18}Y^+$ and $Au_{20}Y^+$ also dimer loss is observed. Note also the odd–even alternations in relative decay probabilities: for odd n Au_nY^+ species a larger monomer metastable decay fraction is recorded than for their even n neighbours. Pronounced maxima in relative fragmentation probability appear at $Au_{17}Y^+$ and $Au_{19}Y^+$ for monomer loss and at $Au_{18}Y^+$ for dimer evaporation.

C. Au_nEr^+

The photofragmentation spectrum for Au_nEr^+ clusters (Fig. 1c) shows intensity steps at $n = 6$ and 16 in addition to an odd–even staggering. The measured dissociation pathways for Au_nEr^+ ($n = 9$–14) are shown in the third column of Fig. 2. The small mass difference between pure gold clusters and erbium doped species prohibited mass selection of Au_nEr^+ solely. Therefore, mass ranges corresponding to Au_{n+1}^+, Au_nEr^+, and $Au_{n-1}Er_2^+$ were selected for $n = 3$–20 (see ESI†), the bare gold being the heaviest. As a consequence, besides fragments stemming from Au_nEr^+, also delayed fragments of bare Au_{n+1}^+ are present. To guide the eye only the delayed fragments of Au_nEr^+ are indicated (labeled arrows). Dimer evaporation is not observed for any of the Au_nEr^+ clusters investigated. The

intensities of $Au_{n-1}Er_2^+$ and their delayed fragments are too low to be able to analyze these species quantitatively. Therefore, these dissociation channels are not indicated and metastable fractions are only deduced for singly doped Au_nEr^+ (see Fig. 3c). Three independent measurements are averaged. Again odd–even alternations in the metastable fractions can be observed. As for Au_nY^+, neutral monomer loss is more likely for Au_nEr^+ containing an odd number of gold atoms and the metastable fraction increases with cluster size.

D. Au_nNb^+

The stability pattern of niobium doped gold clusters (Fig. 1d) shows a pronounced step in intensity at $Au_{14}Nb^+$. In contrast to the findings for Au_nY^+ and Au_nEr^+, no odd–even staggering in the intensity as a function of cluster size is seen for Au_nNb^+. The recorded dissociation pathways for Au_nNb^+ (n = 9–14) are shown in the right column of Fig. 2. The delayed fragmentation of Au_nNb^+ with $n > 14$ could not be monitored, because the cluster intensities were too small. In addition, a perfect mass selection was not always possible and a limited fraction of other species also passed the mass selector. Therefore, a reference signal of pure gold clusters (laser that vaporizes niobium switched off) in the cluster beam was recorded (bottom curves). For all investigated sizes, the only observed delayed fragmentation channel is the gold monomer evaporation, marked with arrows on Fig. 2. The metastable fractions plotted in Fig. 3d were deduced by averaging three independent measurements. In contrast to Au_n^+, Au_nY^+, and Au_nEr^+, no pronounced odd–even staggering or no clear maxima in the metastable fraction as a function of size could be identified.

4. Data analysis

A. Monomer and dimer evaporation rates

In order to establish a relation between mass spectra shaped by evaporation and dissociation energies, an expression for the evaporation rate is needed. Evaporative rate constants are functions primarily of the excitation energy, the evaporative activation energy, and a frequency factor. The main assumption used here is that the decays are activated processes on the experimental time scales of several tens of nanoseconds to hundreds of microseconds. Rate constants are generally given by:[49]

$$k_{n,\Delta n}(E) = \bar{\omega}_{n,\Delta n}\frac{\rho_{n-\Delta n}(E - D_{n,\Delta n})}{\rho_n(E)} \quad (1)$$

where ρ_n and $\rho_{n-\Delta n}$ are the mother and daughter level densities, respectively, Δn = 1, 2 for monomer and dimer decay, E is the excitation energy of the cluster, and $D_{n,\Delta n}$ the dissociation energy for the channel specified, *i.e.*, the energy required to create the daughter cluster from the mother cluster, or the difference in ground state energies of the two:

$$D_{n,\Delta n} = E_{gs}(n - \Delta n) + E_{gs}(\Delta n) - E_{gs}(n) \quad (2)$$

The subscript gs refers to ground state properties. The energy of the free monomer is used as the zero of energy; $E_{gs}(1) = 0$. It is assumed throughout that the dissociation energies equal the evaporative activation energies as is the case if there is no activation energy for the reverse reaction. This is expected to hold for most if not all metal clusters. The frequency factor, $\bar{\omega}_{n,\Delta n}$, depends on the cluster size and the decay channel as indicated by the subscript. It varies with the surface area, *i.e.*, with $n^{2/3}$, and slowly with energy (see ref. 49 for details). These variations are much slower than the variation of the ratio of the level densities, which, for large sizes, develops into a proper Boltzmann factor. The averaging of the frequency factor in eqn (1) refers to setting these slow variations to a constant.

Although the frequency factor is fairly insensitive to the cluster size, it does depend on whether the decay channel is monomer or dimer evaporation. Using eqn (2) a Born–Haber cycle relates two consecutive monomer evaporations to the dimer decay:

$$D_{n,2} - E_{gs}(2) = D_{n,1} + D_{n-1,1} \tag{3}$$

with $-E_{gs}(2) = D_{2,1} = 2.306$ eV the binding energy of the gold dimer.[50]

We will use the level densities of the high energy limit of harmonic oscillators:

$$\rho_n(E) = \frac{(E + E_{0,n})^{3n-7}}{(3n-7)!(\hbar\varpi_D)^{3n-6}} \tag{4}$$

where the Debye frequency of gold, $\varpi_D = 165$ K $k_B/\hbar$, is used as a common vibrational frequency. $E_{0,n}$ is the sum of the zero point energies of the oscillators, *i.e.*, with our use of the Debye frequency $E_{0,n} = 1/2\Sigma_i\hbar\varpi_i \approx 7.2 \times 10^{-3}(3n - 6)$ eV. Incorporation of (4) into (1) gives for the monomer dissociation rate:

$$k_{n,1}(E) \approx \bar{\varpi}_1 \left(\frac{E - D_{n,1} + E_{0,n-1}}{E + E_{0,n}}\right)^{3n-7} \tag{5}$$

with

$$\bar{\varpi}_1' = \bar{\varpi}_1 \left[\frac{(3n-8)\hbar\varpi_D}{E - D_{n,1} + E_{0,n-1}}\right]^3 \tag{6}$$

In ref. 42 a numerical value of $\bar{\varpi}_1' = 3.6 \times 10^{16}$ s^{-1} was derived by setting the last factor in eqn (6) equal to the cube of $\hbar\varpi_D/0.1$ eV. The factor 0.1 eV is a typical daughter temperature. This was shown to be consistent with the experimental values.[42]

The main difference between the monomer and dimer evaporation frequency factors is related to the internal (particularly the rotational) degrees of freedom of the dimer. The rotational constant of Au_2 is $B = B_0 = 0.02636$ cm^{-1} $= 3.3 \times 10^{-6}$ eV.[50] The vibrational quantum energy is $\hbar\varpi_v = 190.9$ cm^{-1} $= 0.02367$ eV. In addition, one has a factor of 2 from the (reduced) mass of the channel, a factor of 1/2 from the symmetry number of the dimer, and a factor of 1/2 from the loss of the electronic degeneracy of the atom. Finally, applying a similar procedure as in eqn (6), one gets the dimer rate constant:

$$k_{n,2}(E) = \bar{\varpi}_2' \left(\frac{E - D_{n,2} + E_{0,n-2}}{E + E_{0,n}}\right)^{3n-7} \tag{7}$$

with

$$\bar{\varpi}_2' = \bar{\varpi}_1' \frac{1}{2} \frac{0.1\,\text{eV}}{B} \frac{0.1\,\text{eV}}{\hbar\varpi_v} \left(\frac{\hbar\varpi_D}{0.1\,\text{eV}}\right)^3 = 186 \cdot \bar{\varpi}_1' \tag{8}$$

This result is obtained by treating the vibrational and rotational degrees of freedom of the dimer as a perturbation, which permits integrating out the energy partitions and expressing the results in terms of canonical partition functions and the daughter microcanonical temperature.

B. Evaporative ensembles

The dependence of evaporative processes on binding energies endows ensembles with information on binding energies. When only one decay channel is present, the analysis is relatively simple but on the other hand only relative values can be found. The analysis can then be based either on the abundances, I_n, or on the amount of

clusters of a certain size that decays in the first field free region of the RTOF mass spectrometer, *i.e.*, the metastable decay fraction, p_n. When both monomer and dimer evaporation occur, experimental branching ratios together with the energy constraint from the Born–Haber cycle allow one to extract absolute values.

To use the theoretical results of the evaporative ensemble each cluster must have undergone at least one evaporation. Furthermore it is required that the energy distribution right after the laser excitation is smooth on the scale set by the dissociation energies.[34] One contributing cause to a broad energy distribution is the Gaussian laser beam profile that gives rise to a broad range of the number of absorbed photons.

When just a single decay channel is active, for simplicity assumed here to be the monomer decay, we can find the highest energy present in the evaporating ensemble at any given time t as:

$$\frac{1}{t} = k_n(E_{\max,n}) \tag{9}$$

which is solved for the energy to give

$$E_{\max,n} = -E_{0,n} + \frac{D_n + E_{0,n} - E_{0,n-1}}{1 - (\bar{\varpi}'_1 t)^{-1/(3n-7)}} \tag{10}$$

If t is chosen as the time when the mass selection occurs during the initial acceleration in the time-of-flight, t_1, one can find the abundances to be proportional to the difference between the highest and lowest energy of size n:[51]

$$\begin{aligned} I_n &\propto E_{\max,n} - E_{\min,n} = E_{\max,n} - (E_{\max,n+1} - D_{n+1}) \\ &= D'_{n+1} + D'_n \frac{1}{1 - (\bar{\varpi}'_1 t)^{-1/(3n-7)}} - D'_{n+1} \frac{1}{1 - (\bar{\varpi}'_1 t)^{-1/(3n-4)}} \end{aligned} \tag{11}$$

where the definition $D'_n \equiv D_n + E_{0,n} - E_{0,n-1} \approx D_n + 0.02$ eV was used. The identification of the lowest energy of cluster size n with the highest energy of size $n + 1$ minus the evaporative activation energy only hinges on the assumption that only the dissociation energy is removed in the process. In other words, that the kinetic energy release is small and there is no reverse activation barrier for the process. The constant of proportionality in eqn (11) is a size dependent but smooth function of n, which contains instrumental parameters like detection efficiency and depends on the kinetics of the cluster formation, *etc*. It can be determined with a primitive application of the method known in nuclear physics as the Strutinsky procedure.[52] The smooth n dependence can be mocked up in a smoothed abundance function, which is then divided out. The procedure leaves an abundance distribution varying around unity, which is used to solve for the dissociation energies numerically. These values are defined only up to a scale factor with smooth size dependence.

It is also possible to calculate the amount of metastable fragmentation. It is given by the amount of decay occurring between the time of initial size selection relative to the time of the laser pulse, t_1, and the time of entry into the reflectron, t_2. With the same constant of proportionality as in eqn (11) it is:

$$p_n \propto E_{\max,n}(t_1) - E_{\max,n}(t_2) \tag{12}$$

The ratio of the metastable fraction to the cluster abundances is therefore:

$$P_n = \frac{p_n}{I_n} = \frac{E_{n,\max}(t_1) - E_{n,\max}(t_2)}{E_{n,\max} - (E_{n+1,\max} - D_{n+1})} \tag{13}$$

As in eqn (11) one may use the rate constants derived above directly in these formulae. It is more transparent to use the rate constant formulated in terms of an

Arrhenius expression. This implies an approximation of the rate constant as:

$$k_n(E) = \bar{\varpi} \exp\left(-\frac{D'_n}{k_B T - D'_n/2C_v}\right) \tag{14}$$

where $k_B T = (E + E_{0,n})/(3n - 7)$ and $C_v = 3n - 7$. The negative term in the denominator of the argument of the exponential is the so-called finite heat bath correction. Both expressions for the rate constants have been used in the analysis described below with practically identical results and we give equations for the Arrhenius expression only. With the above rate constant, the abundances become:

$$I_n \propto \frac{D'_n + D'_{n+1}}{2} - \frac{3D'_{n+1}}{G(t_1)} + \frac{3n-7}{G(t_1)}(D'_n - D'_{n+1}) \tag{15}$$

where G is the Gspann parameter defined as $G(t) = \ln(\bar{\varpi}_1 t)$. The amount of metastable decay becomes:

$$p_n \propto D'_n(3n-7)\left(\frac{1}{G(t_1)} - \frac{1}{G(t_2)}\right) = D'_n(3n-7)\frac{\ln(t_2/t_1)}{(G(t_1)G(t_2))} \tag{16}$$

Combining eqn (15) and (16) gives:

$$\frac{D'_{n+1}}{D'_n} = \left(\frac{(3n-7)\ln(t_2/t_1)}{G(t_1)G(t_2)} - P_n\left(\frac{1}{2} + \frac{3n-7}{G(t_1)}\right)\right) \times \left(P_n\left(\frac{1}{2} - \frac{3n-4}{G(t_1)}\right)\right)^{-1} \tag{17}$$

In this analysis we have disregarded the possibility of radiative cooling. Radiative cooling would manifest itself as a reduced amount of metastable fragmentation, as observed, *e.g.*, for fullerenes in similar experiments.[53] Because the amount of metastable fragmentation was found experimentally to be of the magnitude expected, we conclude that no appreciable radiative cooling was present on the experimental time scales.

C. Dimer dissociation

The presence of competing decay channels complicates the determination of dissociation energies within the evaporative ensemble. The reason is that the branching between the two channels in general depends on the excitation energy. Therefore, the energy density is not constant across the distribution spanned by a single mass. This effect rules out a rigorous use of the concept of "highest and lowest possible excitation energy" used above for monomer decay.

On the other hand, there is an advantage with a competing dimer decay channel, *viz*. the possibility to introduce an absolute energy scale with the help of the Born–Haber cycle. The highest temperature is now determined as:

$$\frac{1}{t} = k_{n,1} + k_{n,2} \approx k_{n,1}(1 + B_n) \tag{18}$$

where B_n is the experimentally determined branching ratio $p_{n,2}/p_{n,1}$. The approximate nature of the last identity is due to the fact that the branching ratio is energy dependent and the observed ratio is therefore a ratio of energy- (or time-) integrated values. However, the correction is small as is best seen if one evaluates the equation below at the two extreme times t_1 and t_2. We will therefore proceed with the identification of the highest temperature with the same relation as above but using a frequency factor modified by the factor $1 + B_n$. The associated Gspann parameter is denoted $G_B(t) = \ln[\bar{\varpi}_1 t(1 + B_n)]$.

Calculating the experimentally observed branching ratio as the ratio of the two rate constants and solving for the ratio of dissociation energies, one gets:

$$\frac{D'_{n,2}}{D'_{n,1}} = \frac{G_B(t_1)^{-1} + (2C_v)^{-1}}{(G_B(t_1) - \ln(B_n\bar{\omega}_1/\bar{\omega}_2))^{-1} + (2C_v)^{-1}} \quad (19)$$

5. Dissociation energies

Eqn (11) and (15) are applied to extract dissociation energies from the experimental data, the result of which is shown in Fig. 4. Relative abundances $I'_n = I_n/\tilde{I}_n$ are used to correct for purely experimental intensity variations as described above. Hereto a simple fitting function was applied: $\tilde{I}_n = Ae^{-Bn}$. Estimated values of t_1 and t_2 were based on electrostatic simulations of the setup (using Simion 3D)[54] and the detection times of the clusters. The reference dissociation energy of the largest investigated size was set to $D_{21} = 1$. The dependence on this initial value is weak. The two expressions of the decay constant k_n, eqn (5) and (14), yield, *via* eqn (11) and (15), similar dissociation energies for all but the smallest sizes. As in the measured abundance spectra, clear steps in the extracted dissociation energies can be seen at specific sizes and an odd–even staggering is present for Au_nX^+ (X = Au, Y, Er).

The ratios of two consecutive dissociation energies, as given by eqn (17), are given in Fig. 5 for Au_n^+, Au_nY^+, Au_nEr^+, and Au_nNb^+ and are compared with the ratios of the dissociation energies obtained with eqn (11) and (15). For a range of Au_n^+ clusters and the high mass range of Au_nY^+ the admixture of dimer decay prevents an analysis in terms of one or both of these methods. The method based on the abundance spectra can be used for all measured Au_nEr^+ and Au_nNb^+ clusters, for Au_nY^+ (n = 3–15) and for Au_n^+ (n = 16–20). The metastable fraction can likewise be used for all measured Au_nEr^+ and Au_nNb^+ clusters, for Au_nY^+ (n = 3–15, 17), and for Au_n^+ (n = 6, 8, 10, 12, 14–19).

Generally, the values obtained with the two methods agree well. There are some features which should be commented on. We note that the uncertainties in the numbers extracted from the abundance spectra are smaller than those involving the

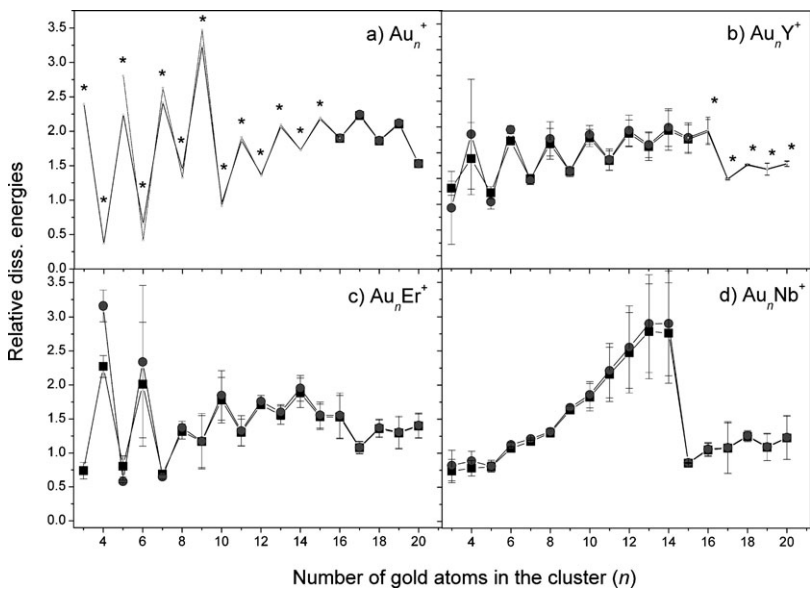

Fig. 4 Relative dissociation energies for (a) Au_n^+, (b) Au_nY^+, (c) Au_nEr^+, and (d) Au_nNb^+, obtained using eqn (11) (black squares) and eqn (15) (gray dots). Sizes marked with an asterisk are uncertain because of the competing dimer decay channel (see text for details).

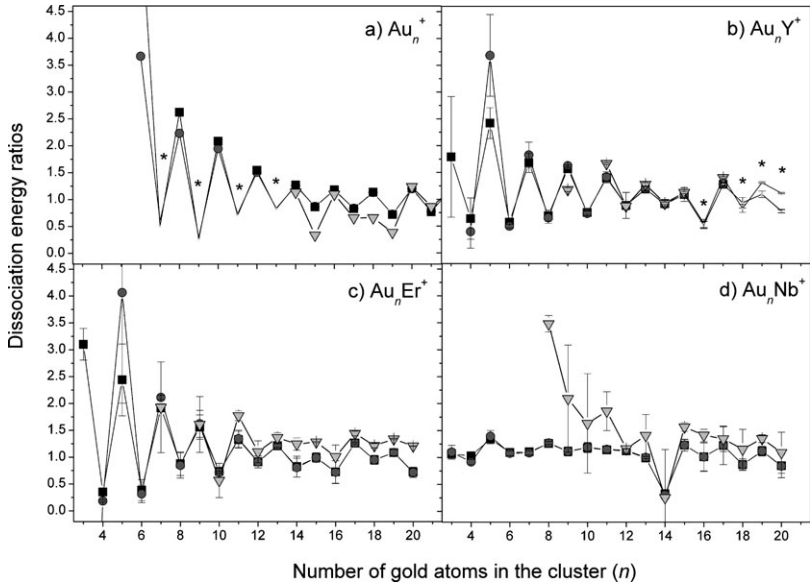

Fig. 5 Ratios of successive dissociation energies, D'_{n+1}/D'_n, for (a) Au_n^+, (b) Au_nY^+, (c) Au_nEr^+, and (d) Au_nNb^+, obtained using eqn (11) (black squares), (15) (gray dots), and (17) (light gray triangles). Sizes marked with an * are uncertain because of the competing dimer decay channel (see text for details).

metastable decay fraction. This is a purely statistical effect due to the small decay fractions. On the other hand there is some amount of arbitrariness involved in the use of the smoothing procedure for the abundances, which is expected to be small but which is difficult to quantify. The general agreement does indicate that the assumptions underlying the analysis are sound, *i.e.*, statistical decays, smooth energy distributions, and heat capacities are consistent with high temperature harmonic oscillator values.

Eqn (19) provides a straightforward way of calculating the fraction of dimer to monomer dissociation energies from the experimental branching ratios. Clear dimer peaks are recorded for Au_n^+ (n = 9, 11, 13, and 15) and Au_nY^+ (n = 18, 20) and the according results are presented in Table 1. The ratios for Au_n^+ are in good agreement with the model-free results presented in ref. 42, which for these cluster sizes are derived and have the relatively high uncertainties of about 10%. It should be noted that the agreement is obtained without any tuning of parameters from data of two distinctly different types of experiments. It should also be noted that a correct treatment of the dimer evaporation rate constant is essential for the agreement. If the

Table 1 Ratio of dimer to monomer dissociation energies, $D'_{n,2}/D'_{n,1}$, obtained with eqn (19) using the experimental branching ratios for Au_n^+ (n = 9, 11, 13, 15) and Au_nY^+ (n = 18, 20). For Au_n^+ also a comparison with model-free values obtained in ref. 42 is given. The * at n = 11 indicates an upper limit based on a monomer branching ratio of 5%. For a branching ratio of 1% the ratio is 1.01

N	$D_{n,2}/D_{n,1}$ (Au_n^+)	$D_{n,2}/D_{n,1}$ (Au_n^+) (ref. 42)	n	$D'_{n,2}/D'_{n,1}$ (Au_nY^+)
9	1.10	1.08	18	1.14
11	1.05*	1.14	20	1.19
13	1.13	1.22		
15	1.18	1.22		

monomer and dimer frequency factors were set equal, as in ref. 33, the ratio would be in error by almost 20%.

The determination of the dimer/monomer dissociation energy allows an absolute determination of the energy for a few cases. The agreement between the present results for pure gold clusters and those presented in ref. 42, shown in Table 1, does not require more comments. For $Au_{18}Y^+$ we use the relation:

$$D'_{n,1} = D'_{2,1}\left(1 + \frac{D'_{n-1,1}}{D'_{n,1}} - \frac{D'_{n,2}}{D'_{n,1}}\right)^{-1} \quad (20)$$

which is derived from the Born–Haber cycle, to find absolute dissociation energies. The values are $D'_{18,1} = 3.25$ eV, $D'_{18,2} = 3.73$ eV, and $D'_{17,1} = 2.78$ eV. As expected the monomer dissociation energy for $n = 18$ is higher than the one for $n = 17$.

6. Discussion

The mother abundances (Fig. 1), the preferred decay channel (Fig. 2), the metastable fractions (Fig. 3), and the calculated dissociation energies (Fig. 4) of the bare and doped gold clusters show a consistent picture that can be interpreted on the basis of an underlying electronic shell structure.

For bare gold clusters (Au = [Xe] $4f^{14}$ $5d^{10}$ $6s^1$) pronounced steps in abundance and dissociation energies are found at $n = 9$ and to a smaller extent at $n = 19$, 21. These observations can be related to a shell structure and magic numbers 8, 18, and 20 that arise from the delocalization of the atomic valence 6s electrons. The electronic structure of the bare gold clusters is also reflected in the metastable fractions for monomer and dimer decay. The tendency of small Au_n^+ ($n < 16$) clusters to decay towards odd-sized clusters, Au_{n-1}^+, by monomer evaporation if n is even and to Au_{n-2}^+ by dimer evaporation if n is odd, can be related to the higher stability of odd-sized gold cluster ions due to their even number of delocalized valence s electrons. Moreover Au_{10}^+ and Au_{20}^+ give a local maximum in the monomer metastable fractions, since they decay to the closed shell Au_9^+ and Au_{19}^+ clusters, respectively.

For Au_nY^+ pronounced maxima in dissociation energies are obtained at Au_6Y^+ and especially $Au_{16}Y^+$ in addition to odd–even alternations. Assuming that each gold atom delocalizes its 6s valence electron, as for pure gold clusters, these cluster sizes correspond to 8 and 18 itinerant electrons, provided that the three yttrium (Y = [Kr] $4d^1$ $5s^2$) valence electrons can be considered itinerant. Also the observation that odd n Au_nY^+ species give a larger monomer decay fraction can be explained as an electronic odd–even effect. The dimer decay that is only recorded for $Au_{18}Y^+$ and $Au_{20}Y^+$ leads to the formation of the closed shell $Au_{16}Y^+$ and $Au_{18}Y^+$ systems. The special stability of $Au_{16}Y^+$ might not only be due to the electronic closed shell (18 electrons) stabilization, but might also be related to a compact and symmetric geometry, similar to the doped golden fullerenes that have been recently predicted for $Au_{16}Cu^-$ and $Au_{17}Cu^-$.[28]

The intensity and dissociation energy (less pronounced) drops after Au_6Er^+ and $Au_{16}Er^+$ in the patterns of Au_nEr^+ clusters can be linked to the magic numbers 8 and 18 assuming that the erbium atom (Er = [Xe] $4f^{12}5d^0$ $6s^2$) delocalizes three valence electrons. The trivalent character of erbium is not surprising, since erbium chemistry is dominated by the trivalent erbium ion Er^{3+} (Er = [Xe] $4f^{11}5d^0$ $6s^0$). The observation of a larger monomer metastable fraction for Au_nEr^+ clusters having an odd number of gold atoms and a maximal metastable fraction for $Au_{17}Er^+$, can be related to the energetic preference for an even amount of itinerant electrons and the decay to the closed shell $Au_{16}Er^+$ system, respectively.

The abundance pattern of Au_nNb^+ is rather smooth and the dissociation energies provide less evidence for an electronic shell structure. No pronounced odd–even staggering is observed neither in the abundance spectra nor in the monomer metastable fractions. Nevertheless, the prominent peak at $Au_{14}Nb^+$ can be explained in terms of an electronic shell closing. In case the niobium atom (Nb = [Kr] $4d^4$ $5s^1$) delocalizes both its 4d and its 5s electrons, $Au_{14}Nb^+$ has in total 18 delocalized electrons.

The appearance of the magic number 18 in the doped gold clusters, at the expense of the magic number 20, which is also present for bare gold, was noted earlier.[7,22] The electronic shell structure in a simple mean field potential with a flat bottom has 20 electrons as a prominent shell closing. However, if the mean field potential has a wine bottle shape, the 2s state is shifted up relative to the 1d level and the magic number 18 becomes more pronounced.[55] The formation of a wine bottle shaped potential can be induced by a centrally located electronegative dopant atom. However, the 18 *versus* 20 competition in gold and doped gold clusters might also have a geometrical origin. It was predicted that the neutral Au_{20} has a tetrahedral geometry and a large HOMO–LUMO gap, representing its electronically closed shell structure.[15,16] The isoelectronic Au_{21}^+ might be composed of tetrahedral neutral Au_{20} with an adatom on a facet. Since Au_{21}^+ is not more pronounced in the fragmentation spectra than Au_{19}^+, its stability is probably not as exceptional as the neutral Au_{20}, confirming that geometric structure does indeed play an important role in determining the cluster stability. Upon doping the clusters with a transition metal, any evidence for the magic number 20 disappears. This might indicate that a tetrahedral geometry (according to the magic number 20) is not stable for the doped clusters, whereas a more spherical caged structure with 18 itinerant electrons (as for $Au_{16}Cu^-$)[28] is.

The dependence of the odd–even effect on the dopant also deserves comment. The preference for dimer *versus* monomer decay in bare gold clusters is controlled by odd–even effects. Clusters with an even number of itinerant electrons are more stable than the ones with an odd number of delocalized electrons. If this stability variation is sufficiently strong, the preferred decay from an even electron numbered cluster will be the dimer decay. This is consistent with the observed correlation between the presence of dimer decay and the strength of the odd–even alternations in the abundances, which are strong for bare gold for which a number of dimer decay channels are observed, less strong for yttrium for which only two sizes evaporate dimers, again somewhat smaller for erbium doped clusters, and finally almost absent for the niobium doped species, the latter two having no observable dimer decay. In the simple mean field picture of shell structure, the odd–even effect is due to structural deviations from spherical symmetry: breaking the symmetry removes the angular momentum degeneracy of levels, leaving just the spin degeneracy of each level. *A priori*, there is no obvious reason why the amplitude of the odd–even effect should be reduced by introducing a dopant atom. Possibly the reason can be found in the specific character of the transition metal (or lanthanide) dopant atom. The valence d electrons are hybridized with the valence s electrons. Since the d electrons have a more localized character, itinerant electron counting is not straightforward. Moreover, the d electron behaviour can be size-dependent, this way reducing the odd or even electron character.[22]

The electronic behaviour of niobium and also of yttrium is very similar to that observed for light 3d transition metal dopant atoms (Sc, Ti, V) in gold clusters. A photofragmentation mass spectrometry study revealed that these dopant atoms contribute both their 4s and 3d electrons to the cloud of itinerant electrons because of the large spatial extent of the corresponding orbitals.[22,23] Since the 4d orbitals of yttrium and niobium are expected to be even larger than the scandium and titanium 3d orbitals, it is not surprising that they show up as delocalized electrons in the present experiments.

7. Conclusion

The dissociation pathways and size-dependent stability of cationic Au_nX^+ (X = Y, Er, and Nb, n = 3–20) clusters produced in a laser vaporization source have been investigated. Photofragmentation experiments were performed with a reflectron time-of-flight mass spectrometer incorporating a wire-type mass gate. Statistical models based on unimolecular decay rates are presented and applied to determine dissociation energies from both the recorded abundances and the fraction of mass selected clusters that undergo delayed fragmentation in the time window of the experiment. Gold monomer evaporation turns out to be the most likely fragmentation channel for doped Au_nX^+, with the exception of $Au_{18}Y^+$ and $Au_{20}Y^+$ for which gold dimer evaporation is a competing channel. The extracted dissociation energies show an odd–even staggering and enhanced stabilities for certain cluster sizes, in agreement with simple electronic shell model predictions.

Acknowledgements

The work in Leuven was supported by the Fund for Scientific Research-Flanders (FWO), the Flemish Concerted Action (GOA/2004/02), and the Belgian Interuniversity Poles of Attraction (IAP/P5/01) programs. E. J. is a postdoctoral researcher of the FWO. K. H. was supported by the Swedish National Research Council (VR).

References

1 M. Haruta, *Gold Bull.*, 2004, **37**, 27.
2 K. J. Taylor, C. L. Pettiette-Hall, O. Cheshnovsky and R. E. Smalley, *J. Chem. Phys.*, 1992, **96**, 3319.
3 C. Jackschath, I. Rabin and W. Schulze, *Ber. Bunsen-Ges. Phys. Chem.*, 1992, **96**, 1200.
4 I. Katakuse, T. Ichihara, Y. Fujita, T. Matsuo, T. Sakurai and H. Matsuda, *Int. J. Mass Spectrom. Ion Processes*, 1985, **67**, 229.
5 M. Lindinger, K. Dasgupta, G. Dietrich, S. Krückeberg, S. Kuznetsov, L. Lützenkirchen, L. Schweikhard, C. Walther and J. Ziegler, *Z. Phys. D*, 1997, **40**, 347.
6 S. Becker, G. Dietrich, H. U. Hasse, N. Klisch, H. J. Kluge, D. Kreisle, S. Krückeberg, M. Lindinger, K. Lützenkirchen, L. Schweikhard, H. Weidele and J. Ziegler, *Z. Phys. D*, 1994, **30**, 341.
7 W. Bouwen, F. Vanhoutte, F. Despa, S. Bouckaert, S. Neukermans, L. T. Kuhn, H. Weidele, P. Lievens and R. E. Silverans, *Chem. Phys. Lett.*, 1999, **314**, 227.
8 H. Häkkinen, M. Moseler, O. Kostko, N. Morgner, M. A. Hoffmann and B. von Issendorff, *Phys. Rev. Lett.*, 2004, **93**, 093401.
9 W. A. de Heer, *Rev. Mod. Phys.*, 1993, **65**, 611.
10 F. Furche, R. Ahlrichs, P. Weis, C. Jacob, S. Gilb, T. Bierweiler and M. M. Kappes, *J. Chem. Phys.*, 2002, **117**, 6982.
11 S. Gilb, P. Weis, F. Furche, R. Ahlrichs and M. M. Kappes, *J. Chem. Phys.*, 2002, **116**, 4094.
12 H. Häkkinen, M. Moseler and U. Landman, *Phys. Rev. Lett.*, 2002, **89**, 033401.
13 V. Bonačić-Koutecký, J. Burda, R. Mitrić, M. Ge, G. Zampella and P. Fantucci, *J. Chem. Phys.*, 2002, **117**, 3120.
14 J. Wang, G. H. Wang and J. Zhao, *Phys. Rev. B*, 2002, **66**, 035418.
15 J. Li, X. Li, H.-J. Zhai and L.-S. Wang, *Science*, 2003, **299**, 864.
16 E. Aprà, R. Ferrando and A. Fortunelli, *Phys. Rev. B*, 2006, **73**, 205414.
17 W. Fa, C. Luo and J. Dong, *Phys. Rev. B*, 2005, **72**, 205428.
18 M. P. Johansson, D. Sundholm and J. Vaara, *Angew. Chem., Int. Ed.*, 2004, **43**, 2678.
19 J. Wang, J. Jellinek, J. Zhao, Z. Chen, R. B. King and P. v. R. Schleyer, *J. Phys. Chem. A*, 2005, **109**, 9265.
20 S. Bulusu, X. Li, L.-S. Wang and X. C. Zeng, *Proc. Natl. Acad. Sci. USA*, 2006, **103**, 8326.
21 Y. Kondo and K. Takayanagi, *Science*, 2000, **289**, 606.
22 S. Neukermans, E. Janssens, H. Tanaka, R. E. Silverans and P. Lievens, *Phys. Rev. Lett.*, 2003, **90**, 33401.
23 E. Janssens, H. Tanaka, S. Neukermans, R. E. Silverans and P. Lievens, *Phys. Rev. B*, 2004, **69**, 085402.
24 E. Janssens, H. Tanaka, S. Neukermans, R. E. Silverans and P. Lievens, *New J. Phys.*, 2003, **5**, 46.

25 H. Tanaka, S. Neukermans, E. Janssens, R. E. Silverans and P. Lievens, *J. Am. Chem. Soc.*, 2003, **125**, 2862.
26 M. B. Torres, E. M. Fernandez and L. C. Balbas, *Phys. Rev. B*, 2005, **71**, 155412.
27 Y. Gao, S. Bulusu and X. C. Zeng, *J. Am. Chem. Soc.*, 2005, **127**, 156801.
28 L. M. Wang, S. Bulusu, H. J. Zhai, X. C. Zeng and L. S. Wang, *Angew. Chem., Int. Ed.*, 2007, **46**, 2915.
29 P. Pyykkö and N. Runeberg, *Angew. Chem., Int. Ed.*, 2002, **41**, 2174.
30 X. Li, B. Kiran, J. Li, H. J. Zhai and L. S. Wang, *Angew. Chem., Int. Ed.*, 2002, **41**, 4786.
31 K. Manninen, P. Pyykkö and H. Häkkinen, *Phys. Chem. Chem. Phys.*, 2005, **7**, 2208.
32 F. Naumkin, *Phys. Chem. Chem. Phys.*, 2006, **8**, 2539.
33 C. Bréchignac, Ph. Cahuzac, J. Leygnier and J. Weiner, *J. Chem. Phys.*, 1989, **90**, 1492.
34 C. E. Klots, *J. Chem. Phys.*, 1985, **83**, 5854.
35 C. Bréchignac, H. Busch, Ph. Cahuzac and J. Leygnier, *J. Chem. Phys.*, 1994, **101**, 6992.
36 C. Bréchignac, Ph. Cahuzac, F. Carlier, M. Defrutos and J. Leygnier, *J. Chem. Phys.*, 1990, **93**, 7449.
37 S. Krückeberg, L. Schweikhard, J. Ziegler, G. Dietrich, K. Lützenkirchen and C. Walther, *J. Chem. Phys.*, 2001, **114**, 2955.
38 V. A. Spasov, T.-H. Lee and K. M. Ervin, *J. Chem. Phys.*, 2000, **112**, 1713.
39 U. Hild, G. Dietrich, S. Krückeberg, M. Lindinger, K. Lützenkirchen, L. Schweikhard, C. Walther and J. Ziegler, *Phys. Rev. A*, 1998, **57**, 2786.
40 V. A. Spasov, T.-H. Lee, J. P. Maberry and K. M. Ervin, *J. Chem. Phys.*, 1999, **110**, 5208.
41 M. Vogel, K. Hansen, A. Herlert and L. Schweikhard, *Phys. Rev. Lett.*, 2001, **87**, 013401.
42 K. Hansen, A. Herlert, L. Schweikhard and M. Vogel, *Phys. Rev. A*, 2006, **73**, 063202.
43 M. Vogel, K. Hansen, A. Herlert and L. Schweikhard, *Eur. Phys. J. D*, 2001, **16**, 73.
44 V. A. Spasov, Y. Shi and K. M. Ervin, *Chem. Phys.*, 2000, **262**, 75.
45 E. Janssens, T. Van Hoof, N. Veldeman, S. Neukermans, M. Hou and P. Lievens, *Int. J. Mass Spectrom.*, 2006, **252**, 38.
46 J. B. Jaeger, T. D. Jaeger and M. A. Duncan, *J. Phys. Chem. A*, 2006, **110**, 9310.
47 W. Bouwen, P. Thoen, F. Vanhoutte, S. Bouckaert, F. Despa, H. Weidele, R. E. Silverans and P. Lievens, *Rev. Sci. Instrum.*, 2000, **71**, 54.
48 P. R. Vlasak, D. J. Beussman, M. R. Davenport and C. G. Enke, *Rev. Sci. Instrum.*, 1996, **67**, 68.
49 K. Hansen, *Philos. Mag. B*, 1999, **79**, 1413.
50 A. M. James, P. Kowalczyk, B. Simard, J. C. Pinegar and M. D. Morse, *J. Mol. Spectrosc.*, 1994, **168**, 248.
51 K. Hansen and U. Näher, *Phys. Rev. A*, 1999, **60**, 1240.
52 V. M. Strutinski, *Nucl. Phys. A*, 1968, **122**, 1.
53 K. Hansen and E. E. B. Campbell, *J. Chem. Phys.*, 1996, **104**, 5012.
54 D. A. Dahl, *Int. J. Mass Spectrom.*, 2000, **200**, 3 (Scientific Instrument Services, Inc., Ringoes, NJ, http://www.simion.com).
55 E. Janssens, S. Neukermans and P. Lievens, *Curr. Opin. Solid State Mater. Sci.*, 2004, **8**, 185.

